Electronic Supplementary Material (ESI) for ChemComm.

A Ferric Guest Inside a Spin Crossover Ferrous Helicate

Leoní A. Barrios,[a,b] Rosa Diego,[a,b] Mohanad Darawsheh,[a] J. I. Martínez,[c,d] Olivier Roubeau*,[c,d] and Guillem Aromí*,[a,b]

Supporting Information

Synthesis of $[Fe(ox)_3]@[Fe_2(L)_3](BF_4)\cdot 3.7H_2O\cdot 4CH_4O$ ($1\cdot 3.7H_2O\cdot 4CH_4O$).
A suspension of L (25 mg, 0.057 mmol) in methanol (10 mL) was added dropwise to methanolic solution (10 ml) of $Fe(BF_4)_2\cdot 6H_2O$ (38.5 mg, 0.114 mmol) and 15 mg of ascorbic acid. A red solution formed which was stirred for 1 hour and then filtered. The resulted filtrate was combined with acetonitrile (15 ml) and the mixture was then left in air for slow evaporation, yielding crystals after two weeks. The yield was 6.1 mg (14.2 %). *Anal. Calc.* (Found) for **1**$\cdot 4.7H_2O\cdot CH_4O$: C, 54.03 (54.28); H, 3.30 (3.67); N, 12.33 (12.52). ESI$^+$-MS: *m/z* 1753.28 ($[Fe(C_2O_4)_3]@[Fe_2L_3])^+$; *m/z* 876.64 ($[Fe(C_2O_4)_3]@[Fe_2L_3] + H^+)^{2+}$.

Crystals of $[Fe(ox)_3]@[Fe_2(L)_3](BF_4)\cdot 3MeOH\cdot 4.75H_2O$ ($2\cdot 3MeOH\cdot 4.75H_2O$)

A methanolic solution of L (20 mg, 0.05 mmol, 10 ml) was added dropwise under nitrogen to a solution of $Fe(BF_4)_2\cdot 6H_2O$ (10.4 mg, 0.031 mmol) in methanol (5 ml) and the resulting solution was stirred for 45 minutes. Following filtration, the filtrate was layered with an aqueous solution of $K_3[V(ox)_3]$ (5 mg).* Crystals were collected after one month and were analyzed by single Crystal X-ray diffraction without isolating the product.

*This reaction was intended to prepare a vanadium analogue of the $[Fe(ox)_3]^{3-}$ guest, but no vanadium could be observed in the analysed crystals.

Single-crystal X-ray diffraction

Data for **1**$\cdot 6CH_3CN\cdot 3H_2O$ were collected at 100 K on an orange rod at BL13-XALOC beamline[1] of the ALBA synchrotron (λ = 0.72932 Å). Data for **2**$\cdot 3CH_4O\cdot 4.75H_2O$ were collected on a red block on Beamline 12.2.1 at the Advanced Light Source (Berkeley, USA), on a Bruker D8 diffractometer equipped with a PHOTON II detector and using silicon (111) monochromated synchrotron radiation (λ = 0.7288 Å). The crystal was mounted with little Paraton N grease on a MiTegen kapton loop and placed in the N_2 stream of an Oxford Cryosystems Cryostream Plus, and measured at 100 K, and then at 280 K. Data reduction and absorption corrections were performed with respectively SAINT and SADABS.[2] All structures were solved by intrinsic phasing with SHELXT[3] and refined by full-matrix least-squares on F^2 with SHELXL.[4] In the structure of **1** a portion of the lattice solvent molecules were too diffuse/disordered to be modelled satisfactorily. The corresponding void spaces were thus analysed and taken into account with PLATON/SQUEEZE,[5] the formula reflecting the squeezed content.

Notes added at the specific request of a crystallographic reviewer:

While the quality of the crystallographic data obtained is not ideal (see below), we are confident that the structural information derived is sufficient to support the conclusions given in the manuscript. In particular, it should be stressed that crystals available for compounds **1** and **2** were not of sufficient size/quality/scattering strength for laboratory diffractometer, so that satisfactory structures could only be obtained using synchrotron radiation sources.

Specifically, a residual density map of the structure of **1** (Figure Sxxx) points at some disorder in the BF_4^- anion and solvent areas. In addition, the F_{obs} *vs.* F_{calc} plot is overall not great, with a large number of reflections showing a relatively poor agreement with the structural model (Figure Sxxx). The latter may in part be a consequence of the fact data were acquired at a synchrotron beamline dedicated to protein crystallography that only allows high-accuracy omega scan and a mini-kappa (0 to 90 degrees). These conditions put limitations on the completeness, especially for a triclinic space group as here. Merging the data acquired at different kappa often brings in overall poorer data reduction quality, while only improving completeness by *ca.* 3% in this specific case. The residual densities/holes observed in the residual density map are likely associated with relatively disordered/diffuse solvent areas always present in these crystals. We refrained from attempting to model these disorders as no relevant information for the purpose of the work would be obtained.

A residual density map of the structure of **2** at 100 K (Figure Sxxx) also points at some likely disorder at the BF_4^- anion, as well as in the solvent areas. These crystals systematically contain relatively disordered/diffuse solvent areas, which content may vary from batch to batch. We believe most of the residual densities/holes observed are related with this and the process of solvent loss during crystal manipulation. We opted to not complicate the structural model since, even if converging satisfactorily, refining the disorder(s) would not add relevant information.

The structure of **2** at 280 K suffers from the effect of higher temperature data acquisition, and a relatively large number of outliers are seen in the F_{obs} *vs.* F_{calc} plot (Figure Sxxx). We hypothesize that this is mostly related with the crystal progressively damaging during acquisition, as a consequence of solvent areas become more and more diffuse. In any case, we are again confident that the quality of the structural information obtained is sufficient to support the conclusions drawn in the manuscript.

All details can be found in CCDC 2159592 (**1**, T = 100 K), 2121784 (**2**, *T* = 100 K), 2121794 (**2**, *T* = 280 K), which contain the supplementary crystallographic data for this paper. These data can be obtained free of charge from The Cambridge Crystallographic Data Center via https://summary.ccdc.cam.ac.uk/structure-summary-form. Crystallographic and refinement parameters are summarized in Table S1 together with average Fe–N bond lengths.

Differential Scanning Calorimetry (DSC)

Experiments were done with a Q1000 calorimeter from TA Instruments equipped with the LNCS accessory on polycrystalline samples enclosed in a crimped Al pan, at a scanning rate of 10 $Kmin^{-1}$. The temperature and enthalpy scales were calibrated with a standard sample of In. For heat capacity, a synthetic sapphire was measured in the same temperature range, giving an overall accuracy of 0.2 K in *T* and up to 10% in heat capacity. The excess heat capacity associated to the SCO process in **1** was obtained after subtraction of the lattice heat capacity estimated fitting a 4th order polynomial function to the low and high temperature data (dashed lined in Figure 3 left). The excess enthalpy and entropy were then obtained by integration of the excess heat capacity over *T* and ln*T* respectively.

Magnetometry

Variable-temperature magnetic measurements were performed using a Quantum Design MPMS-XL SQUID magnetometer at the “Unitat de Mesures Magnètiques” of the

Universitat de Barcelona, using polycrystalline samples, with a constant magnetic field of 0.5 T. Measurements were done in settle mode, in which the temperature is stabilized at each set-point before the measurement is taken, the temperature being varied at 5 K/min between each set-points, resulting in an average scan rate of *ca.* 0.8 K/min. Note that this is not at all equivalent to the scan rate used in sweep mode measurements, in which the temperature is not stabilized before the measurement is taken. LIESST experiments and *ac* susceptibility measurements were done with a commercial magnetometer equipped with a SQUID sensor hosted by the Physical Measurements Unit of the Servicio General de Apoyo a la Investigación-SAI, Universidad de Zaragoza. The diamagnetic contributions to the susceptibility were corrected using Pascal's constant tables. Further corrections of the sample holders contribution, determined empirically, were also applied. Variable temperature *dc* data were collected with an applied field of 5000 Oe, in settle mode. *ac* data were collected with a 4 Oe field oscillating at different frequencies in the range $1 \leq \nu \leq 1420$ Hz.

Electron Paramagnetic Resonance (EPR) spectroscopy

X-band EPR measurements were performed on a deuterated frozen solution of compound **1** (0.25 mM, DMSO-d_6:MeOH-d_4:EtOH-d_6, 1:36:4) with a Bruker Biospin ELEXSYS E-580 spectrometer using a gas-flow Helium cryostat for low-temperature experiments. Simulation of the spectra was done with Easyspin.[6]

Other Physical Measurements

Elemental analyses were performed with a Perkin-Elmer Series II CHNS/O Analyzer 2400 (C, H, N) at the Servei de Microanàlisi of CSIC, Barcelona. IR spectra were recorded as KBr pellet samples on a Nicolet 5700 FTIR spectrometer. ESI mass spectrometry was carried out using a LC/MSD-TOF spectrometer (Agilent Technologies) equipped with an electrospray ionization (ESI) source at the Serveis Cientificotècnics of the Universitat de Barcelona.

Table S1. Crystal data and average Fe−N or Fe−O bond lengths for **1** and its polymorph **2**. For comparison, the unit cell for the Cr(III) analogue compound **3** at 100 K is *a* = 19.4808(6) Å, *b* = 16.5141(5) Å, *c* = 28.6823(9) Å, *β* = 109.611(2)° and *V* = 8692.1(5) Å^3, thus very similar to that of **2**.

	1·$6CH_3CN·3H_2O$	**2**·$3CH_4O·4.75H_2O$	
Formula	$Fe_2C_{84}H_{60}N_{18}$, FeC_6O_{12}, BF_4, 6(C_2H_3N), 3(H_2O)	$Fe_2C_{84}H_{60}N_{18}$, FeC_6O_{12}, BF_4, 3(CH_4O), 4.75(H_2O)	
FW (g mol^{-1})	2140.28	2021.62	
T (K)	100	100	280
Wavelength (Å)	0.72932	0.7288	
Crystal system	triclinic	monoclinic	
Space group	*P*–1	$P2_1/n$	
a (Å)	14.8701(8)	19.6737(16)	20.122(8)
b (Å)	18.4351(11)	16.6758(13)	16.557(6)
c (Å)	18.8758(12)	28.868(3)	28.572(12)
α (°)	75.913(2)	90	90
β (°)	84.722(2)	109.814(3)	109.976(3)
γ (°)	79.764(2)	90	90
V (Å^3)	4932.5(5)	8910.2(14)	8946(6)
Z	2	4	
ρ_{calcd} (g cm^{-3})	1.441	1.507	1.501
μ (mm^{-1})	0.574	0.611	0.608
Independent reflections (R_{int})	119650 (0.0527)	21201 (0.0417)	10834 (0.0504)
parameters / restraints	1351 / 205	1289 / 29	1178 / 228
Goodness-of-fit	1.020	1.026	1.058
Final R1 / wR2 [I>2σ(I)]	0.0876 / 0.2578	0.0742 / 0.2172	0.1234 / 0.3373
Final R1 / wR2 [all data]	0.0934 / 0.2644	0.0796 / 0.2214	0.1359 / 0.3599
largest diff. peak / hole (e Å^3)	1.471 / –0.691	1.530 / –0.952	0.813 / –1.290
<Fe1–N> (Å)	1.98(2)	1.97(2)	1.98(3)
<Fe2–N> (Å)	1.97(2)	1.98(2)	2.15(5)
<Fe3–O> (Å)	2.05(2)	2.05(2)	2.03(4)

Table S2. Selected hydrogen bonding in the structures of **1** and **2** at 100 K. Only those hydrogen bonds involved in the host-guest interaction or in the H-bonded network of iron tris-oxalate are shown. For comparison pyrazole-oxalate N···O distances in the structure of **3** at 100 K are very similar to those in **1**, ranging 2.866-3.038 Å, while the oxalate-water O···O distances are significantly longer, ranging 2.755-3.014 Å.

D–H···A	D–H (Å)	H···A (Å)	D–A (Å)	D–H···A (º)
1				
N3–H3···O9	0.88	2.23	2.994(5)	145.3
N4–H4···O6	0.88	2.23	2.994(5)	145.5
N9–H9···O5	0.88	2.09	2.871(4)	147.3
N10–H10···O2	0.88	2.44	3.181(5)	141.6
N15–H15···O1	0.88	2.15	2.917(5)	145.8
N16–H16···O10	0.88	2.13	2.922(5)	148.9
O1W···O4	-	-	2.746(5)	-
O2W···O11	-	-	2.665(5)	-
O3W···O8	-	-	2.639(5)	-
O3W···O3W#1	-	-	2.977(5)	-
2				
N3–H3···O1	0.88	2.62	3.306(4)	135.1
N3–H3···O1W	0.88	2.07	2.816(4)	141.7
N4–H4···O11	0.87(5)	1.98(5)	2.847(4)	171(4)
N9–H9···O5	0.90(5)	2.22(5)	3.035(4)	151(4)
N10–H10···O3	1.04(5)	1.76(5)	2.796(4)	170(4)
N15–H15···O9	0.83(5)	2.29(5)	3.052(4)	153(4)
N16–H16···O7	0.86(5)	2.04(5)	2.842(4)	153(5)
O1W–H1WA···O2	0.953(19)	1.82(2)	2.768(4)	174(5)
O1W#1–H1WB···O2	0.928(19)	2.08(3)	2.949(4)	155(4)

#1: 1-x, 1-y, 1-z; #2: 1-x, -y, 1-z

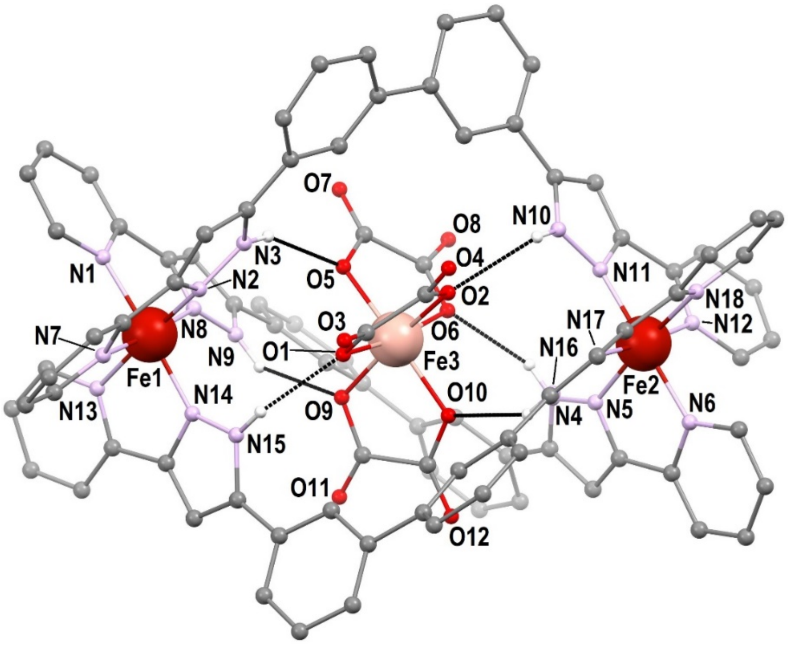

Figure S1. Representation of the supramolecular ($[Fe(ox)_3]@[Fe_2L_3]$)$^+$ cationic moiety of **1**, with heteroatoms labelled, emphasizing the H-bonding interactions (black dashed lines, see Table S2 for details) between the central $[Fe(ox)_3]^{3-}$ guest and the $[Fe_2L_3]^{4+}$. Only H atoms from N−H groups shown.

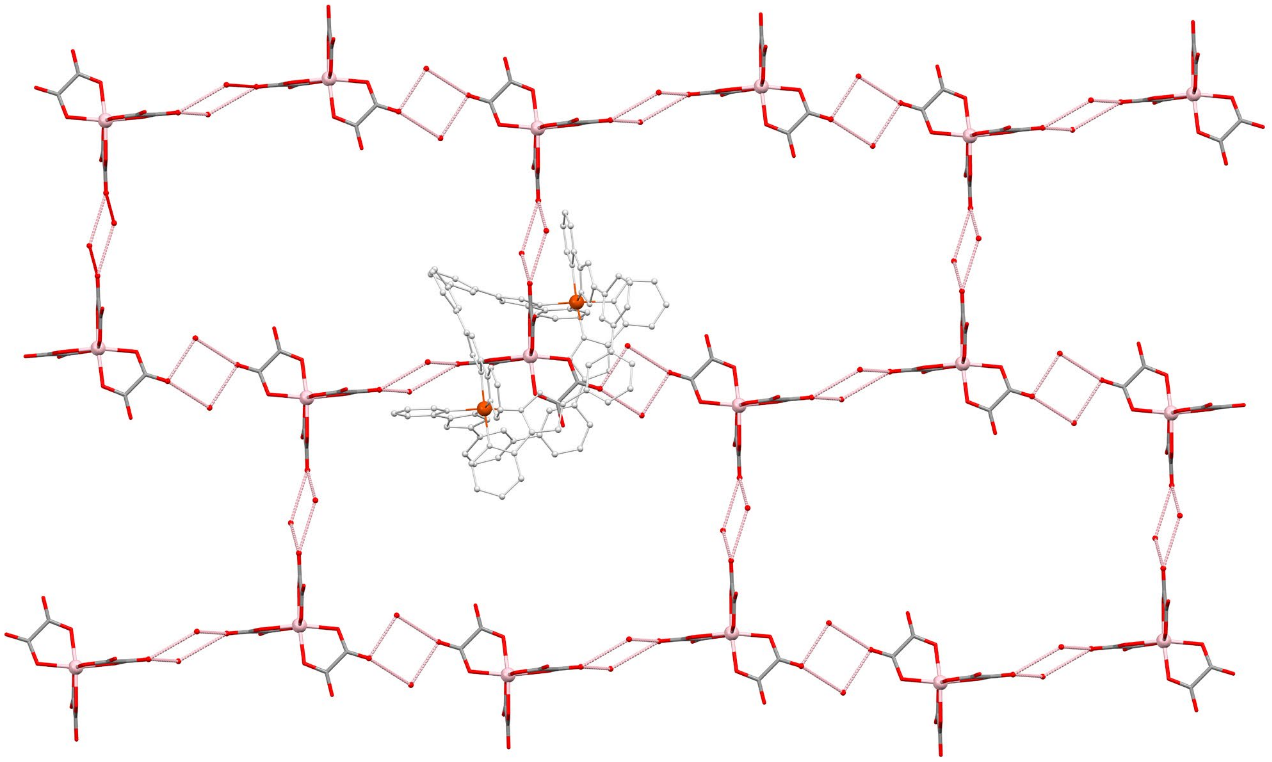

Figure S2. Representation of the 2D hydrogen bonding (pink dashed lines) network within the lattice of **1**·$6CH_3CN·3H_2O$ formed by the $[Fe(ox)_3]^{3-}$ moieties and water molecules of crystallization (see Table S2 for details). One of the $[Fe(ox)_3]^{3-}$ complexes is shown with the $[Fe_2L_3]^{4+}$ host surrounding it (with grey atoms, except Fe(II) which are red). H atoms not shown.

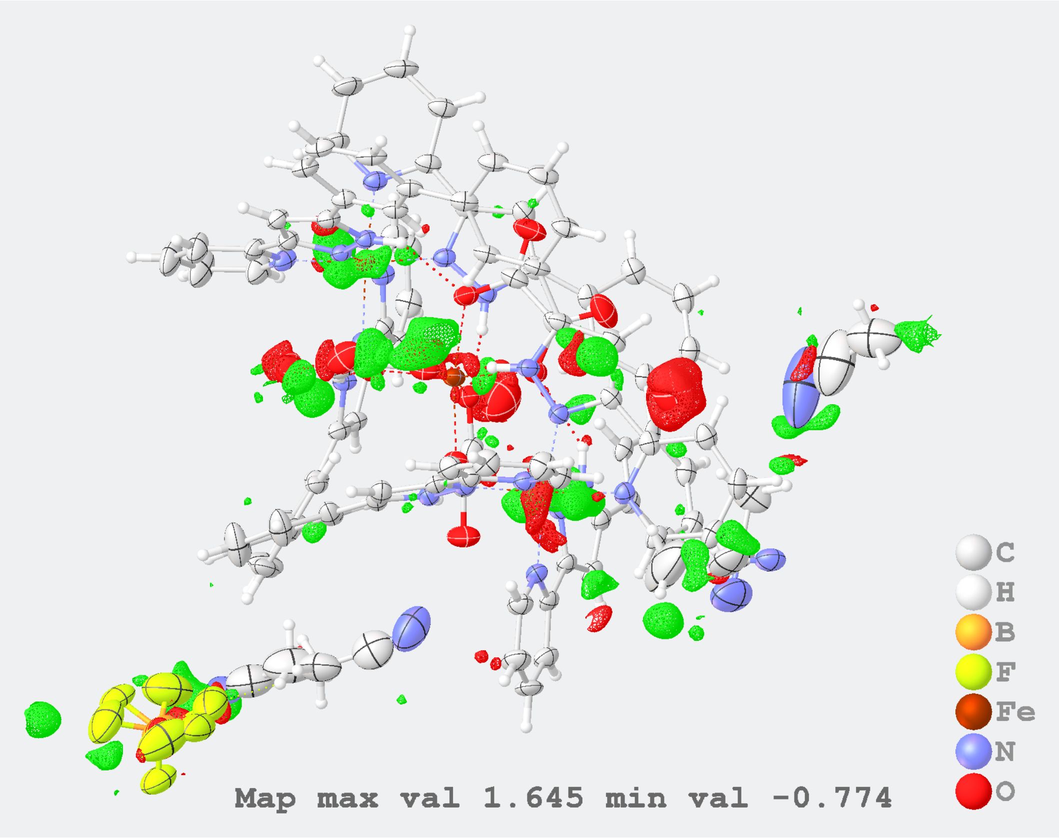

Figure S3. Residual density map for the structure of **1**, indicating the presence of disorder both at the BF_4^- anion and in the lattice solvent areas.

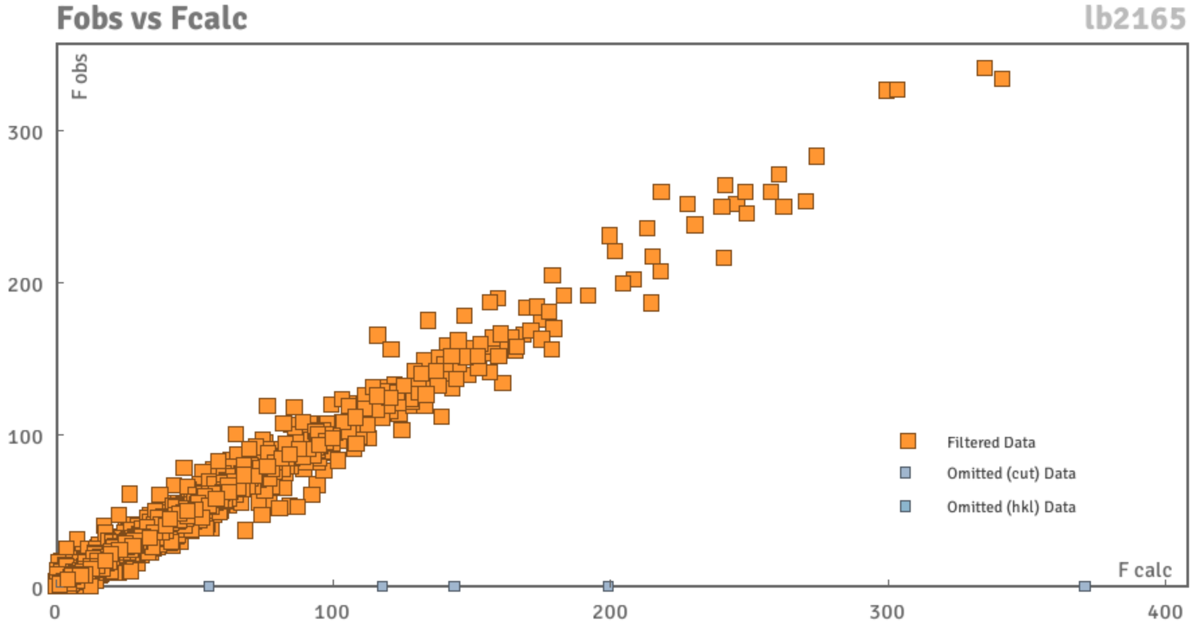

Figure S4. Fobs *vs.* Fcalc plot for the structure of **1**.

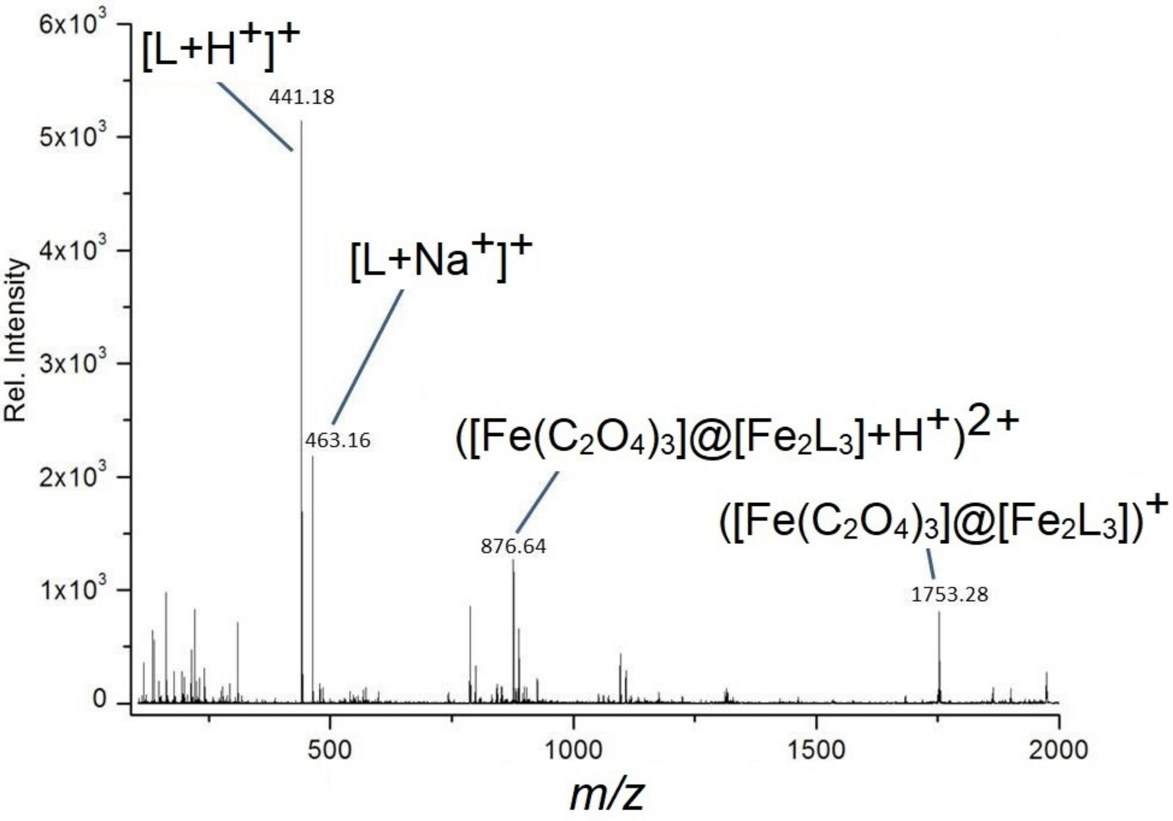

Figure S5. Positive electrospray ionization mass spectrogram (MS) of **1** confirming the stability of the ([Fe(ox)$_3$]@[Fe$_2$L3])$^+$ assembly in solution of DMSO/acetonitrile.

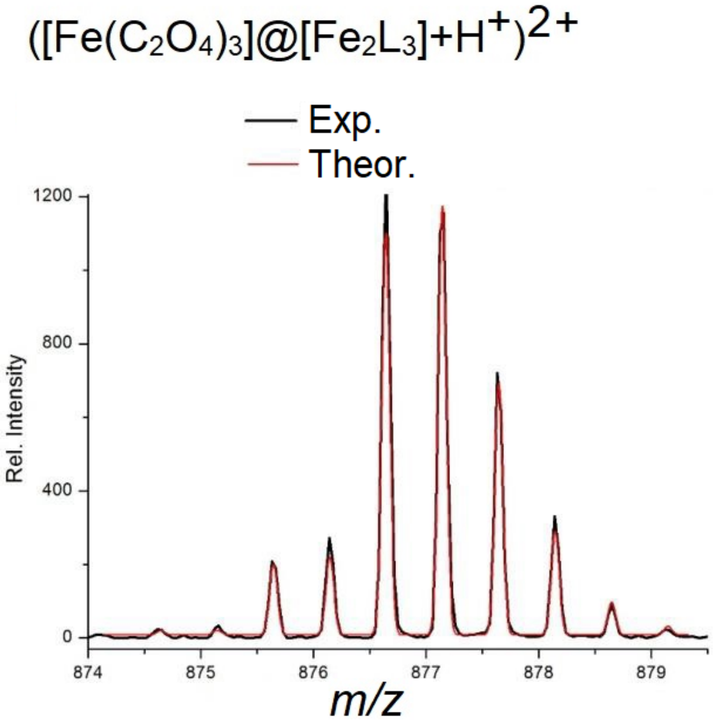

Figure S6. Portion of the above MS, recorded for **1**, sowing the experimental (red) and calculated (blue) isotopic distributions, for the peak corresponding to [M+H]$^{2+}$ (*m/z* = 876.64).

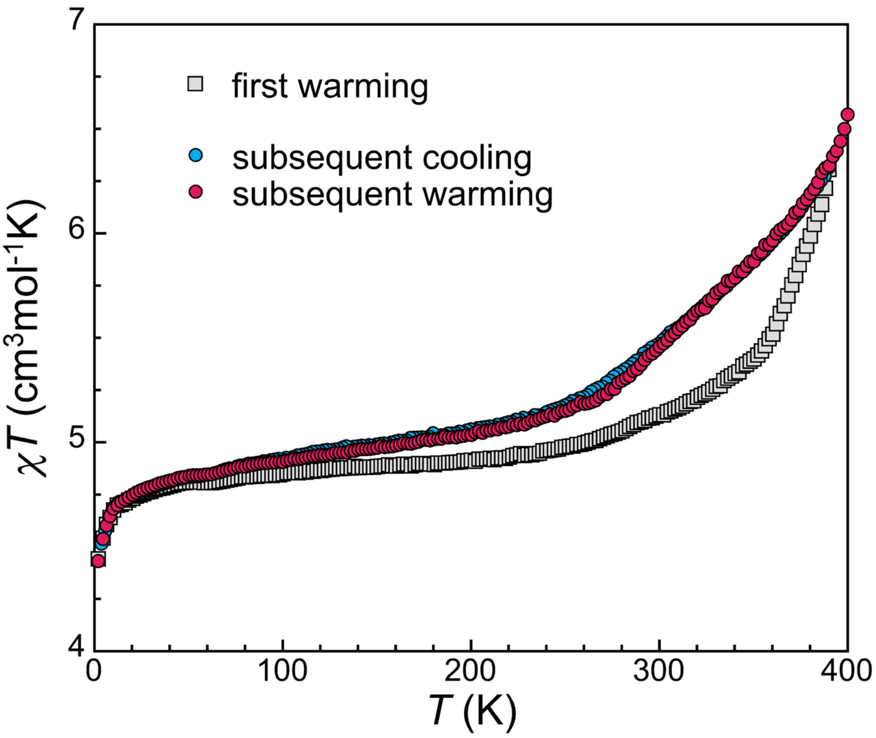

Figure S7. Temperature dependence of the χT product of compound **1** in an applied dc field of 5000 Oe for two successive thermal cycles as indicated. The first cooling from 300 to 2 K is not shown for clarity as it is identical to the first warming. Further thermal cycles do not alter the properties observed for the second cycle.

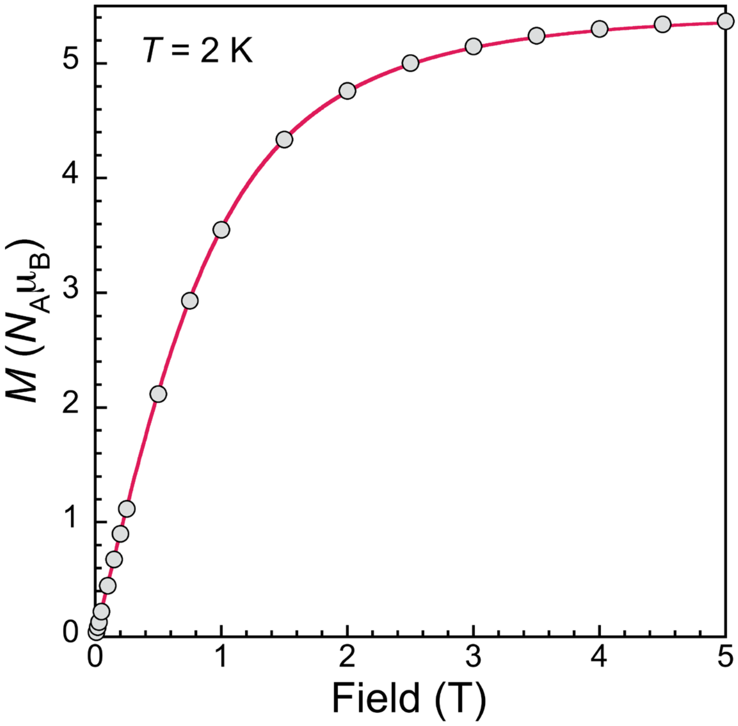

Figure S8. Magnetization *vs.* field for **1** at *T* = 2 K. The full red line is the Brillouin function for *S* = 5/2, *g* = 2.165 and *T* = 2 K.

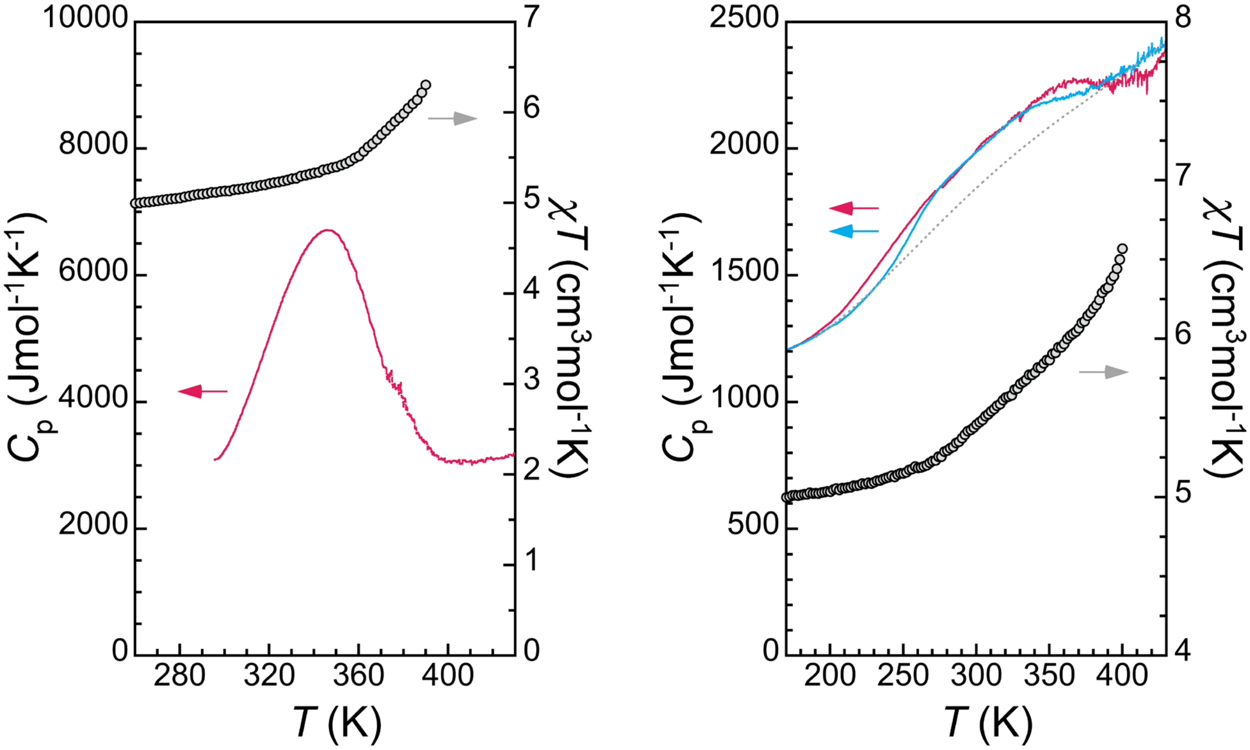

Figure S9. Comparison of the temperature dependence of the heat capacity C_p derived from DSC measurements with that of the χT product. Left: first warming ramp. Right: second cycle. Red/blue lines depict warming/cooling branches. With such very broad anomalies, the definition of a lattice heat capacity to estimate the SCO excess heat capacity is difficult. A more confident estimation was obtained with the data upon cooling (using a 4th order polynomial function) and is shown as a dashed line.

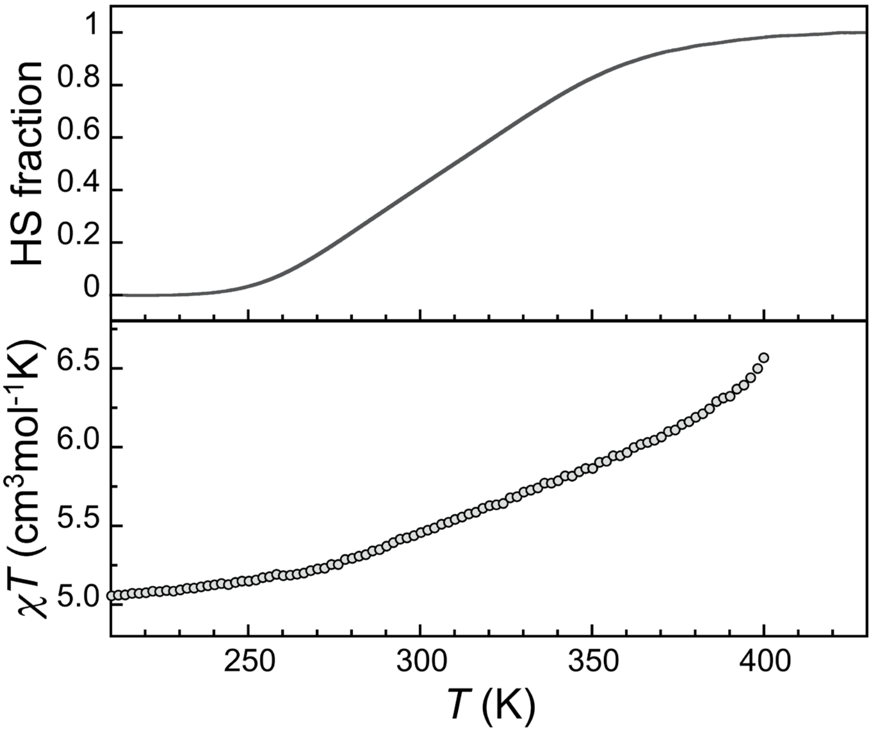

Figure S10. Comparison of the temperature dependence of (top) HS fraction at the Fe site exhibiting SCO as derived from DSC data considering $\gamma_{HS}(T) = \Delta H(T)/\Delta_{SCO}H$ and (bottom) the χT product.

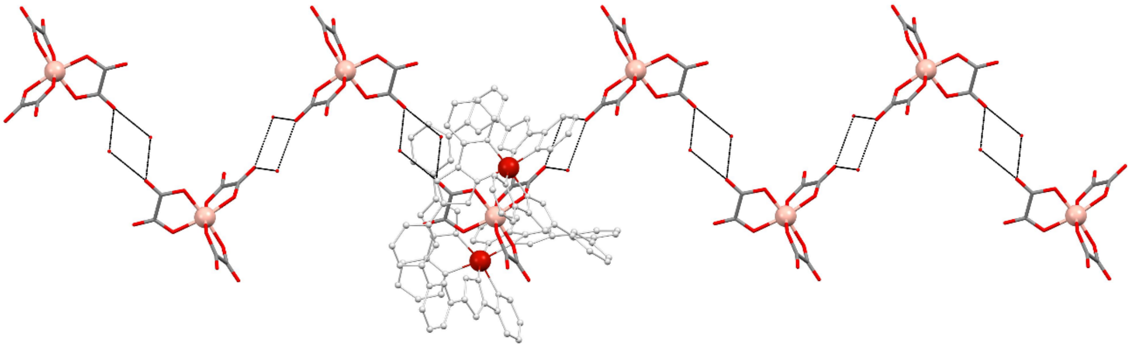

Figure S11A. Representation of the 1D hydrogen bonding (black dashed lines) network within the lattice of **2**·$3CH_4O$·4.75·H_2O, formed by the $[Fe(ox)_3]^{3-}$ moieties and water molecules of crystallization. One of the $[Fe(ox)_3]^{3-}$ complexes is shown with the $[Fe_2L_3]^{4+}$ host surrounding it (with grey atoms, except Fe(II) which are red). H atoms not shown.

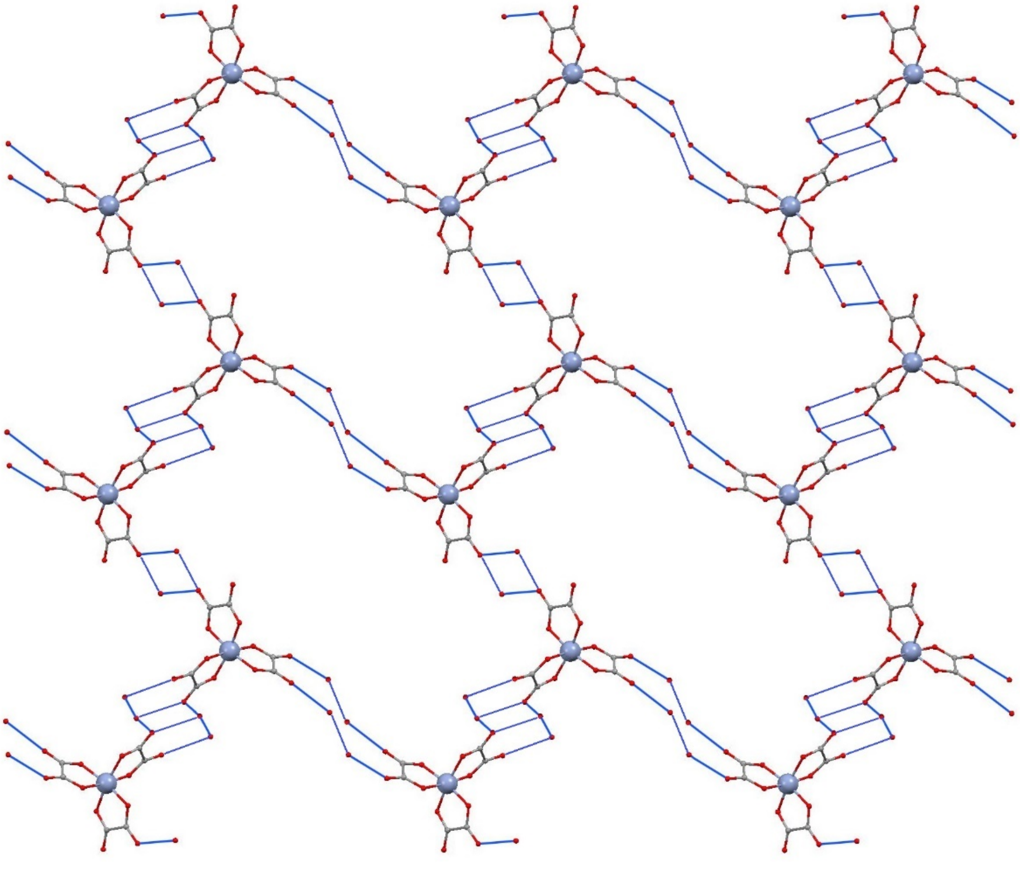

Figure S11B. Representation of the 2D hydrogen bonding network within the lattice of **3**, formed by the $[Cr(ox)_3]^{3-}$ moieties and the water molecules of crystallization (six per anion). Hydrogen bonds are shown as blue lines. Notice the same 1D chains as observed in **2** formed through single water molecule bridges. The further connection of these through two water molecules is not observed in **2**, but the packing is very similar.

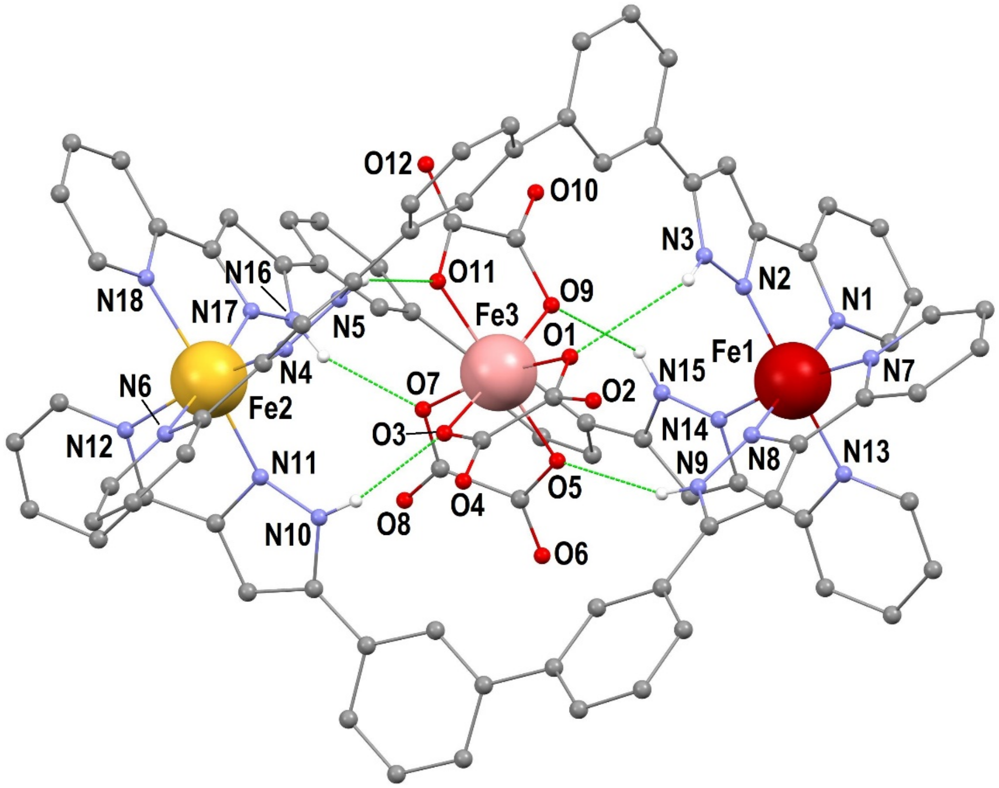

Figure S12. Representation of the supramolecular ($[Fe(ox)_3]@[Fe_2L_3]$)$^+$ cationic moiety in **2**, at 280 K with heteroatoms labelled, emphasizing the different spin states of Fe(II); Fe1 is in LS and Fe2 in the HS state. H-bonding interactions (green dashed lines, see Table S2 for details) between the central $[Fe(ox)_3]^{3-}$ guest and the $[Fe_2L_3]^{4+}$. Only H atoms from N−H groups shown.

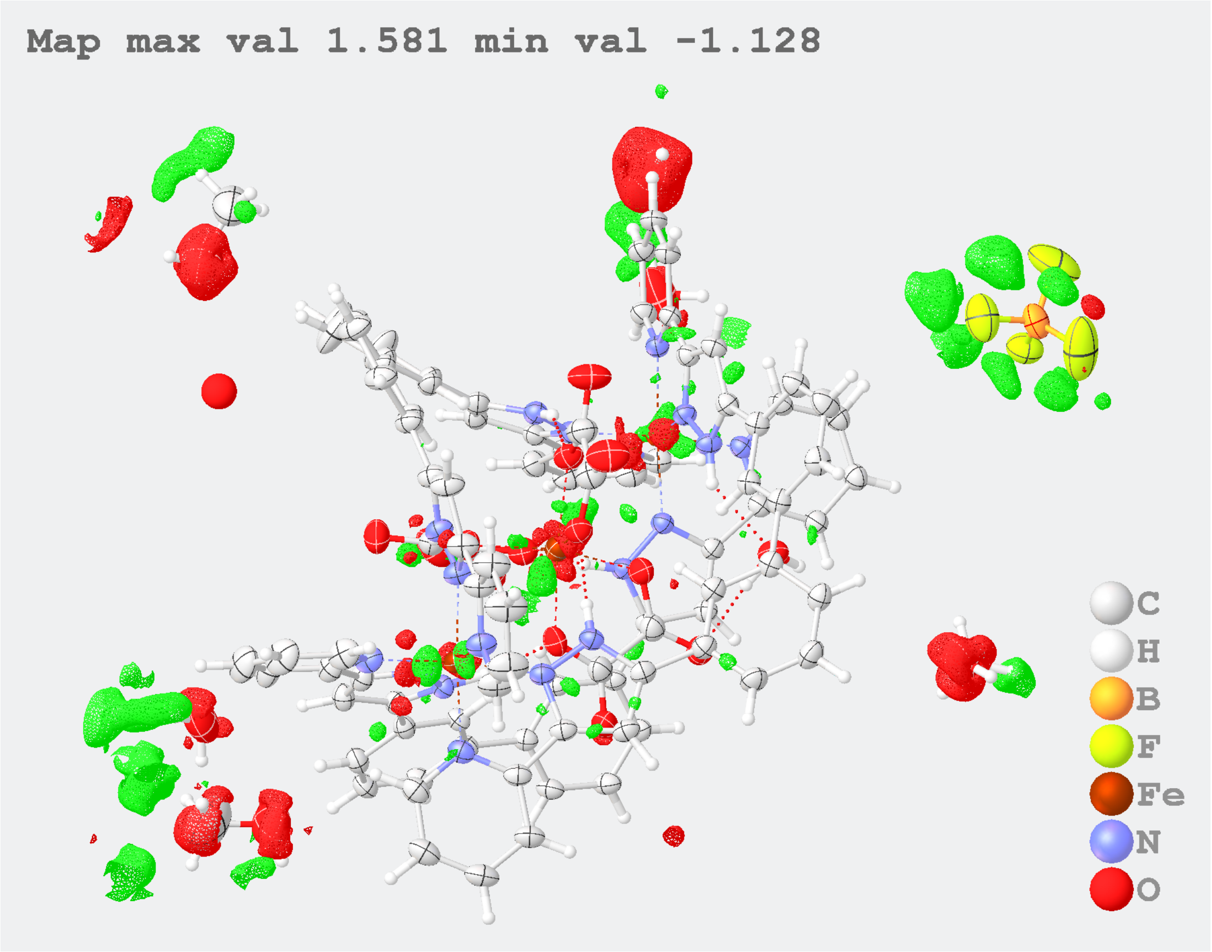

Figure S13. Residual density map for the structure of **2** at 100 K, indicating the presence of disorder both at the BF_4^- anion and in the lattice solvent areas.

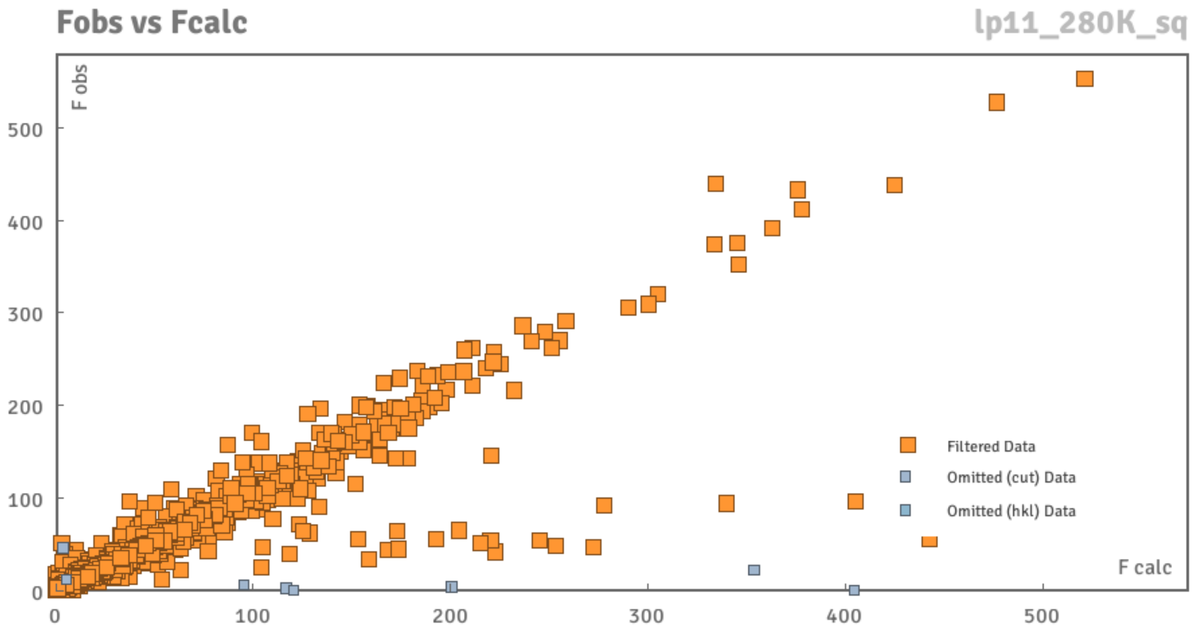

Figure S14. Fobs *vs.* Fcalc plot for the structure of **2** at 280 K.

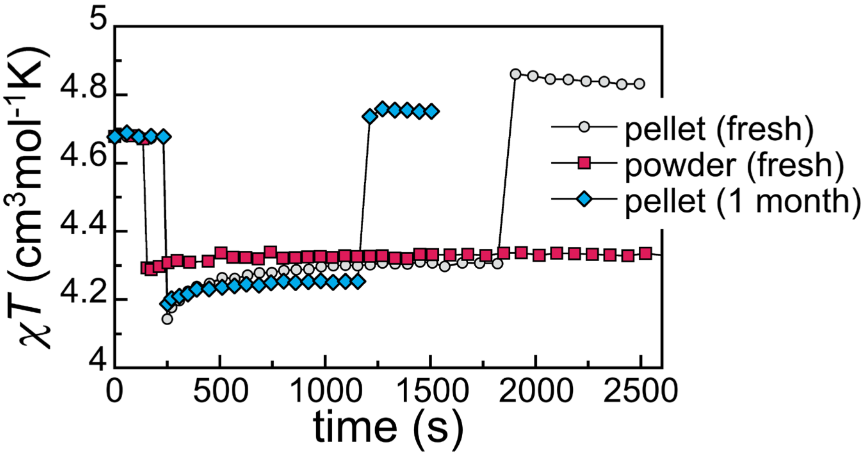

Figure S15. Variation of χT with time upon turning on and off the 500-600 nm lamp, at T = 10 K and for three different samples of compound **1**, as indicated: a thin pellet made from fresh polycrystalline solid, the same fresh polycrystalline solid and a thin pellet made of the polycrystalline solid after *ca.* 1 month in contact with air.

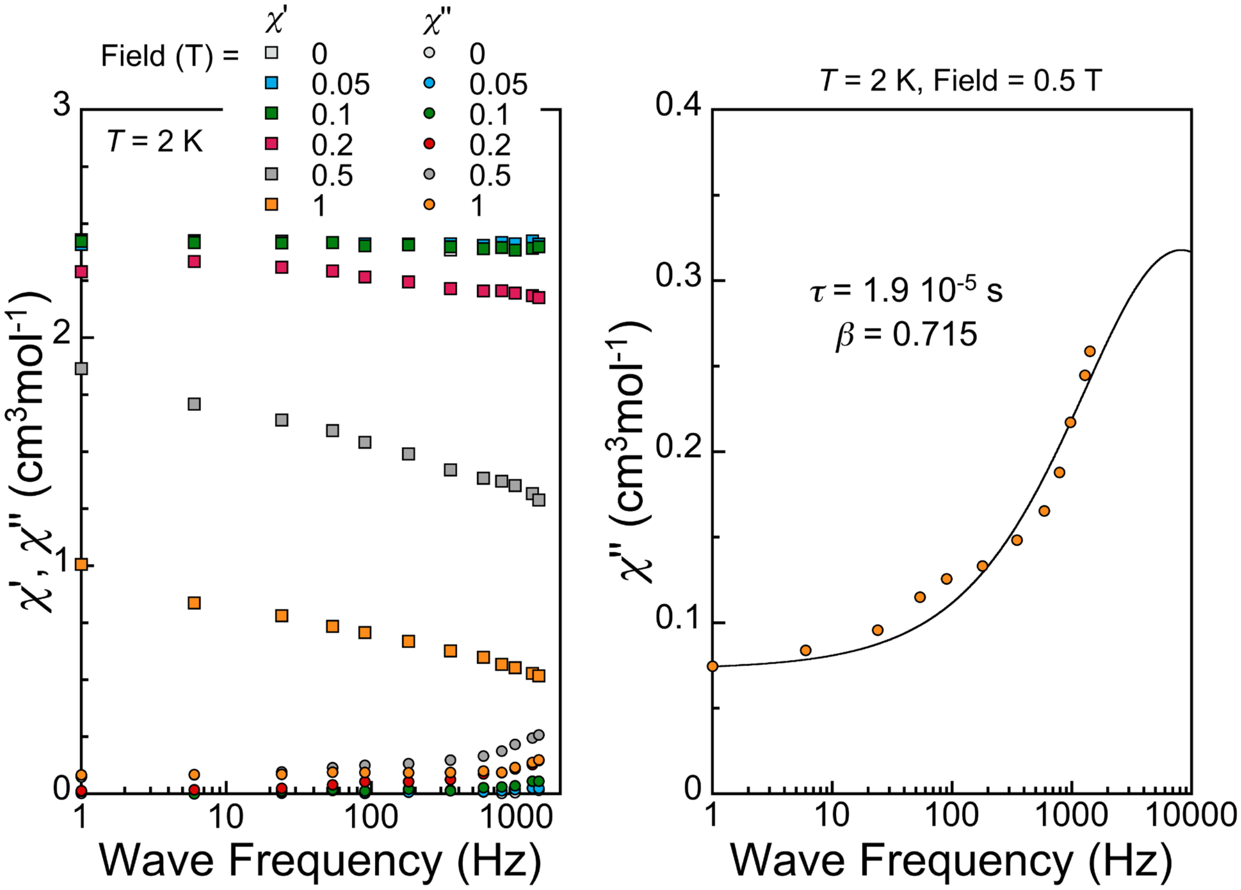

Figure S16. Left: frequency dependence of the in-phase (squares) and out-of-phase (circles) *ac* magnetic susceptibility of **1** at T = 2 K and the indicated applied dc fields, evidencing the onset of an out-of-phase component at the higher frequencies and thus sow relaxation of magnetization. Right: out-of-phase ac susceptibility at 5000 Oe dc field and its fit (full line) to the generalized Debye model expression of the imaginary susceptibility data:

$$\chi^{"}(\omega) = (\chi_T - \chi_S)\frac{(\omega\tau)^{\beta}\sin\left(\frac{\pi\beta}{2}\right)}{1 + 2(\omega\tau)^{\beta}\cos\left(\frac{\pi\beta}{2}\right) + (\omega\tau)^{2\beta}}$$

in which ω is the angular frequency, χ_{T} the isothermal susceptibility, χ_{S} the adiabatic susceptibility and β describes the distribution of relaxation times.

References

[1] J. Juanhuix, F. Gil-Ortiz, G. Cuní, C. Colldelram, J. Nicolás, J. Lidón, E. Boter, C. Ruget, S. Ferrer and J. Benach, *J. Synchrotron Radiat.*, 2014, **21** , 679-689

[2] G. M. Sheldrick, *SAINT and SADABS*, 2012, Bruker AXS Inc., Madison, Wisconsin, USA.

[3] G. M. Sheldrick, *Acta Cryst. A* 2015, **71**, 3-8.

[4] G. M. Sheldrick, *Acta Cryst. C* 2015, **71**, 3-8.

[5] A. L. Spek, *Acta Cryst. C* 2015, **71**, 9-18.

[6] S. Stoll, A. Schweiger, *J. Magn. Reson.* 2006, **178**, 42